Quasi-Stationary North Finding with a FOG-Based IMU

Theory, Sensor Requirements, and a Quaternion Error-State Kalman Filter

Rasit Evduzen

October 2026

Abstract

North finding by gyrocompassing determines the azimuth of an instrument from the Earth's rotation rate sensed by its own gyroscopes, without any external reference. Because the horizontal component of the Earth rate is only $15.04^\circ/\mathrm{h}\cos L$ at latitude L, the achievable accuracy is governed by the bias stability and the noise of the gyroscopes. In addition, practical installations are rarely perfectly still. This paper gives a self-contained treatment of quasi-stationary north finding. Starting from the reference frames and the measurement model of a stationary inertial measurement unit (IMU), the analytic leveling and gyrocompassing equations are derived together with a closed-form heading error budget, from which the sensor requirements for a target accuracy and alignment time are obtained. A noise identification procedure based on the Allan variance and the power spectral density links the measured sensor noise to the process noise of the estimator. Fine alignment is performed by a quaternion error-state Kalman filter that processes zero-velocity pseudo-measurements and models the vibration of the support as a Gauss-Markov disturbance. An observability analysis explains why the attainable accuracy is bounded by the east gyro bias. The method is evaluated on a 60 s record of a fiber-optic gyroscope (FOG) IMU at 40.92° N. The filter estimates the heading as 342.70° with a 1σ uncertainty of 0.88°, in agreement with the error budget, in which the $0.1^\circ/\mathrm{h}$ gyro bias sets a floor of 0.50°. A Monte Carlo simulation confirms that this uncertainty is realistic. The analytic gyrocompass gives 343.13°, and the difference is traced to a slow drift of the horizontal specific force, to which the filter is sensitive and plain averaging is not.

Keywords North finding, gyrocompassing, quasi-stationary alignment, error-state Kalman filter, quaternion, fiber-optic gyroscope, Allan variance.

1 Introduction

North finding is the determination of the angle between a reference axis of an instrument and true north. It is required whenever an instrument has to be pointed or a navigation system has to be initialized without an external azimuth reference, for example in the orientation of artillery and launchers, the pointing of antennas and optical instruments, land and borehole surveying, tunneling, and the initial alignment of inertial navigation systems. Magnetic compasses are disturbed by local magnetic fields and require a declination model, celestial methods need a clear sky, and satellite-based heading needs open sky and a two-antenna baseline. Gyrocompassing avoids all of these limitations. A set of gyroscopes measures the Earth rotation vector, whose horizontal component points to true north, and accelerometers measure gravity, which defines the vertical. The method is self-contained and works in any weather and indoors.

The difficulty of gyrocompassing lies in the size of the signal. The Earth rotates at $\Omega = 15.041^\circ/\mathrm{h}$, and only its horizontal component $\Omega\cos L$, which is $11.365^\circ/\mathrm{h}$ at $L = 40.92^\circ$, carries the azimuth information. A gyro bias of $0.1^\circ/\mathrm{h}$, a small number for most applications, already corresponds to a heading error of about 0.5°. The accuracy of north finding is therefore determined by the quality of the gyroscopes, and the selection of the sensor is as important as the estimation algorithm.

Alignment is usually carried out in two stages [7, 15]. *Coarse alignment* computes the attitude analytically from the averaged accelerometer and gyro outputs, and *fine alignment* refines it with a Kalman filter that also estimates the sensor errors. Depending on the motion of the host, one distinguishes

stationary, quasi-stationary, and in-motion alignment. In *stationary* alignment the IMU is perfectly still with respect to the Earth, and long averaging of the sensor outputs is nearly optimal. In *quasi-stationary* alignment the host stays at the same place on average but is subject to small disturbing motions, such as the vibration of the floor or of running machinery, wind buffeting, people moving on board, or the swaying of a moored ship. These motions enter the sensor outputs as genuine signals and corrupt plain averages. The standard remedy is a Kalman filter that processes zero-velocity pseudo-measurements, which express the knowledge that the mean velocity is zero, while it treats the residual motion as noise [7]. In *in-motion* alignment the rotation of the vehicle dominates the Earth rate, and external aiding such as satellite navigation or transfer alignment from a master system is required.

The fine-alignment filter of this paper is an error-state (indirect) Kalman filter [6, 7]. The nominal attitude is carried by a unit quaternion, and the filter estimates a small three-dimensional attitude error that is fed back multiplicatively [12, 14, 16]. This combination keeps the covariance minimal and well conditioned, and it avoids both the singularities of Euler angles and the normalization constraint of a quaternion state.

This paper develops quasi-stationary north finding from first principles and validates it on real data. It makes five contributions.

1. A self-contained derivation from the reference frames and the stationary IMU model to analytic leveling and gyrocompassing and to a closed-form heading error budget that separates gyro noise, gyro bias, and accelerometer bias.
2. Sensor requirements for a target heading accuracy and alignment time, and their translation into sensor grades.
3. A noise identification procedure based on the Allan variance and the power spectral density that maps the measured noise to the process noise of the filter.
4. A quaternion error-state Kalman filter for quasi-stationary alignment with zero-velocity pseudo-measurements and a Gauss-Markov disturbance model, together with an observability analysis that explains the gyro-bias limit of the accuracy.
5. An experimental evaluation with a 60 s record of a FOG IMU, supported by a Monte Carlo simulation, which explains the difference between the filter and the analytic gyrocompass by a slow drift of the horizontal specific force.

The paper is organized as follows. Section 2 introduces the reference frames, the attitude representations, and the measurement model of a stationary IMU. Section 3 derives leveling, gyrocompassing, and the heading error budget, and Section 4 turns the budget into sensor requirements. Section 5 describes the noise identification. Section 6 presents the quaternion error-state Kalman filter and its observability. Section 7 reports the experimental results, and Section 8 concludes the paper.

2 Reference Frames, Attitude, and the Stationary IMU

2.1 Reference frames

Four right-handed frames are used [7]. The *inertial frame i* has its origin at the Earth's center and axes fixed with respect to the stars, and its z axis is the Earth's rotation axis. The *Earth frame e* shares the origin and the z axis but rotates with the Earth at the rate Ω. The *local navigation frame n* is centered at the instrument with its axes pointing north, east, and down (NED), where down is the direction of gravity. The *body frame b* is fixed to the IMU with x forward, y to the right, and z down when the instrument is level. The heading ψ is the angle from true north to the horizontal projection of the body x axis. It is positive clockwise when seen from above, which is a positive rotation about the down axis.

A stationary IMU rotates with the Earth. The only rotation its gyroscopes measure with respect to inertial space is the Earth rate, and the only specific force its accelerometers measure is the reaction to gravity. Gyrocompassing extracts the attitude, including the heading, from these two known vectors.

2.2 Attitude representations

The direction cosine matrix (DCM) $\mathbf{C}_b^n$ transforms a vector from body to navigation axes, $\boldsymbol{v}^n = \mathbf{C}_b^n \boldsymbol{v}^b$, with $\mathbf{C}_n^b = (\mathbf{C}_b^n)^\top$. In terms of the heading ψ, pitch θ, and roll ϕ, applied as successive rotations about the z, y, and x axes,

$$\mathbf{C}_b^n = \mathbf{R}_z(\psi)\mathbf{R}_y(\theta)\mathbf{R}_x(\phi) = \begin{bmatrix} c_\theta c_\psi & -c_\phi s_\psi + s_\phi s_\theta c_\psi & s_\phi s_\psi + c_\phi s_\theta c_\psi \\ c_\theta s_\psi & c_\phi c_\psi + s_\phi s_\theta s_\psi & -s_\phi c_\psi + c_\phi s_\theta s_\psi \\ -s_\theta & s_\phi c_\theta & c_\phi c_\theta \end{bmatrix}, \tag{1}$$

where $c_\alpha = \cos\alpha$ and $s_\alpha = \sin\alpha$. The angles follow from $\phi = \operatorname{atan2}(C_{32}, C_{33})$, $\theta = -\arcsin C_{31}$, and $\psi = \operatorname{atan2}(C_{21}, C_{11})$.

The filter carries the attitude as the unit quaternion $\mathbf{q} = \mathbf{q}_b^n = [q_0,\, q_1,\, q_2,\, q_3]^\top$ with scalar part q_0. With $\boldsymbol{\rho}$ a rotation vector of angle $\|\boldsymbol{\rho}\|$ about the axis $\boldsymbol{\rho}/\|\boldsymbol{\rho}\|$, the corresponding quaternion is

$$\mathbf{q}(\boldsymbol{\rho}) = \begin{bmatrix} \cos(\|\boldsymbol{\rho}\|/2) \\ \sin(\|\boldsymbol{\rho}\|/2)\, \boldsymbol{\rho}/\|\boldsymbol{\rho}\| \end{bmatrix}, \tag{2}$$

and the Hamilton product of $\mathbf{p} = [p_0,\, \mathbf{p}_v^\top]^\top$ and $\mathbf{q} = [q_0,\, \mathbf{q}_v^\top]^\top$ is

$$\mathbf{p} \otimes \mathbf{q} = \begin{bmatrix} p_0 q_0 - \mathbf{p}_v^\top \mathbf{q}_v \\ p_0 \mathbf{q}_v + q_0 \mathbf{p}_v + \mathbf{p}_v \times \mathbf{q}_v \end{bmatrix}. \tag{3}$$

The DCM of a unit quaternion is

$$\mathbf{C}(\mathbf{q}) = \begin{bmatrix} q_0^2 + q_1^2 - q_2^2 - q_3^2 & 2(q_1 q_2 - q_0 q_3) & 2(q_1 q_3 + q_0 q_2) \\ 2(q_1 q_2 + q_0 q_3) & q_0^2 - q_1^2 + q_2^2 - q_3^2 & 2(q_2 q_3 - q_0 q_1) \\ 2(q_1 q_3 - q_0 q_2) & 2(q_2 q_3 + q_0 q_1) & q_0^2 - q_1^2 - q_2^2 + q_3^2 \end{bmatrix}, \tag{4}$$

and products compose like rotations, $\mathbf{C}(\mathbf{p} \otimes \mathbf{q}) = \mathbf{C}(\mathbf{p})\,\mathbf{C}(\mathbf{q})$, so that the right factor is applied first. With $\boldsymbol{e}_1$, $\boldsymbol{e}_2$, and $\boldsymbol{e}_3$ the unit vectors along the x, y, and z axes, the quaternion of the Euler angles in (1) is $\mathbf{q} = \mathbf{q}(\psi \boldsymbol{e}_3) \otimes \mathbf{q}(\theta \boldsymbol{e}_2) \otimes \mathbf{q}(\phi \boldsymbol{e}_1)$, which gives

$$\mathbf{q} = \begin{bmatrix} c_{\phi/2} c_{\theta/2} c_{\psi/2} + s_{\phi/2} s_{\theta/2} s_{\psi/2} \\ s_{\phi/2} c_{\theta/2} c_{\psi/2} - c_{\phi/2} s_{\theta/2} s_{\psi/2} \\ c_{\phi/2} s_{\theta/2} c_{\psi/2} + s_{\phi/2} c_{\theta/2} s_{\psi/2} \\ c_{\phi/2} c_{\theta/2} s_{\psi/2} - s_{\phi/2} s_{\theta/2} c_{\psi/2} \end{bmatrix}. \tag{5}$$

The heading follows directly from the quaternion as $\psi = \operatorname{atan2}\big(2(q_0 q_3 + q_1 q_2),\, 1 - 2(q_2^2 + q_3^2)\big)$. Finally, $[\,\boldsymbol{a}\times]$ denotes the skew-symmetric matrix with $[\,\boldsymbol{a}\times]\boldsymbol{b} = \boldsymbol{a} \times \boldsymbol{b}$.

2.3 Earth rotation and gravity

In NED axes at latitude L the Earth rotation vector is

$$\boldsymbol{\omega}_{ie}^n = \Omega \begin{bmatrix} \cos L \\ 0 \\ -\sin L \end{bmatrix}, \qquad \Omega = 7.2921 \times 10^{-5}\ \text{rad/s} = 15.041^\circ/\text{h}. \tag{6}$$

Its north component $\Omega \cos L$ is the signal of gyrocompassing. Its vertical component $-\Omega \sin L$ is fixed by the latitude and serves as a consistency check. At $L = 40.92^\circ$ the two components are $11.365^\circ/\text{h}$ and $-9.853^\circ/\text{h}$, and Fig. 1(a) illustrates the decomposition. Gravity points down, $\boldsymbol{g}^n = [0,\, 0,\, g]^\top$. Its magnitude is given by the Somigliana model of the WGS-84 ellipsoid with a free-air height correction [7,13],

$$\begin{aligned} g(L,h) &= g_0(L)\left[1 - \frac{2}{R_0}\left(1 + f\,(1 - 2\sin^2 L) + \frac{\Omega^2 R_0^2 R_P}{\mu}\right)h + \frac{3h^2}{R_0^2}\right], \\ g_0(L) &= 9.7803253359\,\frac{1 + 0.001931853\sin^2 L}{\sqrt{1 - e^2 \sin^2 L}}\ \text{m/s}^2, \end{aligned} \tag{7}$$

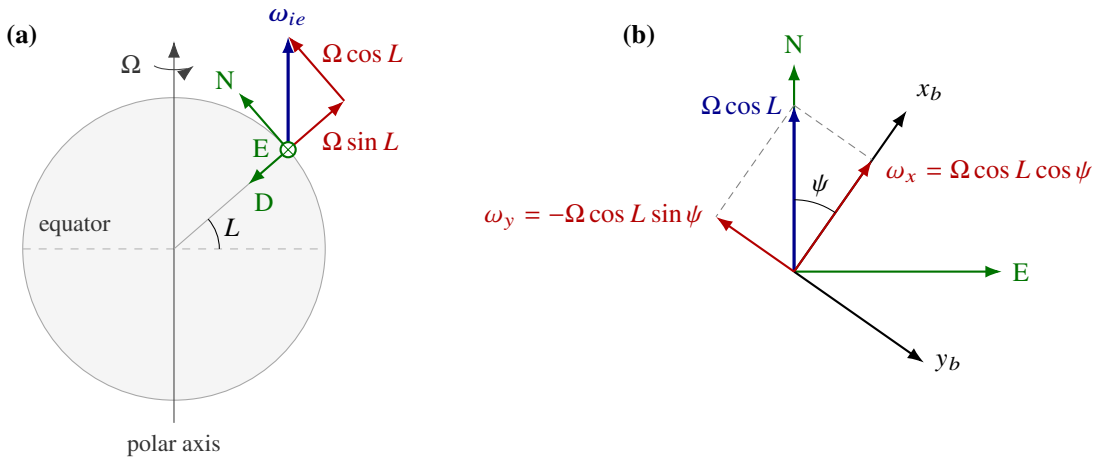


Figure 1. Geometry of gyrocompassing. (a) Meridian plane through the instrument at latitude L. The Earth rotation vector $\boldsymbol{\omega}_{ie}$ is parallel to the polar axis and splits into a north component $\Omega\cos L$ and an upward component $\Omega\sin L$. The east axis E of the local NED frame points into the page. (b) Horizontal plane seen from above for a level body with heading ψ. The horizontal Earth rate points north, and the gyros along the body x and y axes measure its projections $\omega_x = \Omega\cos L\cos\psi$ and $\omega_y = -\Omega\cos L\sin\psi$. For $0 < \psi < 180^\circ$ the y_b axis points away from north, so ω_y is negative and its vector component is drawn along $-y_b$. This sign tells on which side of north the body x axis lies, and the ratio of the two projections gives the heading.

where R_0 and R_P are the equatorial and polar radii, f is the flattening, e the eccentricity, μ the Earth's gravitational constant, and h the height. A body at rest experiences the specific force $\boldsymbol{f}^n = -\boldsymbol{g}^n = [0,\ 0,\ -g]^\top$, which points up.

2.4 Measurement model of a stationary IMU

The gyroscopes measure the angular rate of the body with respect to inertial space, and the accelerometers measure the specific force, both resolved in body axes. For an IMU at rest,

$$\tilde{\boldsymbol{\omega}}_{ib}^b = \mathbf{C}_n^b \boldsymbol{\omega}_{ie}^n + \boldsymbol{b}_g + \boldsymbol{w}_g, \tag{8}$$

$$\tilde{\boldsymbol{f}}^b = \mathbf{C}_n^b \boldsymbol{f}^n + \boldsymbol{b}_a + \boldsymbol{w}_a, \tag{9}$$

where $\boldsymbol{b}_g$ and $\boldsymbol{b}_a$ are slowly varying biases and $\boldsymbol{w}_g$ and $\boldsymbol{w}_a$ are wide-band noises (Section 5). Under quasi-stationary conditions both outputs also contain the small zero-mean angular and linear motion of the support. The attitude $\mathbf{C}_b^n$, and in particular the heading, is the unknown of north finding.

3 Analytic Alignment by Leveling and Gyrocompassing

Let $\bar{\boldsymbol{f}}$ and $\bar{\boldsymbol{\omega}}$ denote the averages of the accelerometer and gyro outputs over an interval of length T. Averaging suppresses the noise and the zero-mean disturbing motion but not the biases.

3.1 Leveling

Substituting $\boldsymbol{f}^n = [0,\ 0,\ -g]^\top$ and (1) into (9) without errors gives

$$\boldsymbol{f}^b = -g\,\mathbf{C}_n^b \boldsymbol{e}_3 = g \begin{bmatrix} \sin\theta \\ -\sin\phi\cos\theta \\ -\cos\phi\cos\theta \end{bmatrix}, \tag{10}$$

which does not depend on the heading. Roll and pitch therefore follow from the averaged specific force,

$$\phi = \operatorname{atan2}\big(-\bar{f}_y,\ -\bar{f}_z\big), \qquad \theta = \arctan\frac{\bar{f}_x}{\sqrt{\bar{f}_y^2 + \bar{f}_z^2}}, \tag{11}$$

which is valid for any roll and $|\theta| < 90°$ [7].

3.2 Gyrocompassing

Write the attitude as $\mathbf{C}_b^n = \mathbf{R}_z(\psi)\,\mathbf{C}_b^\ell$ with the heading-free leveling matrix $\mathbf{C}_b^\ell = \mathbf{R}_y(\theta)\mathbf{R}_x(\phi)$, which is known after leveling. Resolving the averaged angular rate in the level frame ℓ and using (8) gives

$$\boldsymbol{\omega}^\ell = \mathbf{C}_b^\ell \bar{\boldsymbol{\omega}} = \mathbf{R}_z(\psi)^\top \boldsymbol{\omega}_{ie}^n = \Omega \begin{bmatrix} \cos L \cos\psi \\ -\cos L \sin\psi \\ -\sin L \end{bmatrix}. \tag{12}$$

The first two components are the projections of the horizontal Earth rate on the level body axes (Fig. 1(b)), and their ratio gives the heading,

$$\psi = \operatorname{atan2}\big(-\omega_y^\ell,\, \omega_x^\ell\big), \qquad \begin{aligned} \omega_x^\ell &= \bar{\omega}_x \cos\theta + (\bar{\omega}_y \sin\phi + \bar{\omega}_z \cos\phi)\sin\theta, \\ -\omega_y^\ell &= -\bar{\omega}_y \cos\phi + \bar{\omega}_z \sin\phi, \end{aligned} \tag{13}$$

which is independent of the magnitude of Ω and of $\cos L$. The third component of (12) must equal $-\Omega \sin L$. Equivalently, the vertical component of the measured rate, $\bar{\boldsymbol{\omega}}^\top \bar{\boldsymbol{f}}/\|\bar{\boldsymbol{f}}\|$, must equal $\Omega \sin L$, and it therefore implies the latitude $\arcsin\big(\bar{\boldsymbol{\omega}}^\top \bar{\boldsymbol{f}}/(\Omega\|\bar{\boldsymbol{f}}\|)\big)$. Together with $\|\bar{\boldsymbol{f}}\| = g$, this checks the vertical channels and the relative sign convention of the gyros and accelerometers. A sign error on the vertical channel of either sensor makes the implied latitude negative. The check is blind to the assignment of the horizontal axes, for example to a rotation of both sensor triads by 180° about the vertical, which must therefore come from the markings of the housing.

3.3 Heading error budget

Let $\delta\boldsymbol{\omega}^n$ be an error of the averaged rate resolved in NED and $\delta\boldsymbol{\omega}^\ell = \mathbf{R}_z(\psi)^\top \delta\boldsymbol{\omega}^n$ the same error in the level frame. Linearizing (13) about the true heading gives $\delta\psi = -(\cos\psi\,\delta\omega_y^\ell + \sin\psi\,\delta\omega_x^\ell)/(\Omega\cos L)$. Since the east component of the error is $\delta\omega_E = \sin\psi\,\delta\omega_x^\ell + \cos\psi\,\delta\omega_y^\ell$, this is

$$\delta\psi = -\frac{\delta\omega_E}{\Omega\cos L}. \tag{14}$$

Any error that looks like an east rotation is interpreted as a heading error. Three sources contribute.

Gyro noise. White rate noise of density N_i on body axis i averages to a standard deviation $N_i/\sqrt{T}$. Its east projection has the density $N_E = \big(\sum_i (C_b^n)_{2i}^2 N_i^2\big)^{1/2}$, so that

$$\sigma_{\psi,N} = \frac{N_E}{\Omega\cos L\,\sqrt{T}}. \tag{15}$$

Gyro bias. A constant bias with east component $b_{g,E}$ is not reduced by averaging and causes

$$\delta\psi_b = -\frac{b_{g,E}}{\Omega\cos L}, \tag{16}$$

which amounts to 5.04° per 1°/h at $L = 40.92°$.

Accelerometer bias. An east accelerometer bias $b_{a,E}$ tilts the computed level frame about north by the angle $b_{a,E}/g$. The tilt rotates part of the vertical Earth rate into the east axis, $\delta\omega_E = -\Omega\sin L\, b_{a,E}/g$, and (14) gives

$$\delta\psi_a = \frac{b_{a,E}}{g}\tan L. \tag{17}$$

This term is small. A bias of 0.5 mg causes only 0.025° at $L = 40.92°$.

Treating the biases as random with standard deviations σ_{bg} and σ_{ba}, the heading uncertainty of analytic gyrocompassing is

$$\sigma_\psi^2(T) = \left(\frac{N_E}{\Omega\cos L\,\sqrt{T}}\right)^2 + \left(\frac{\sigma_{bg}}{\Omega\cos L}\right)^2 + \left(\frac{\sigma_{ba}\tan L}{g}\right)^2. \tag{18}$$

Here σ_{bg} is the uncertainty of the gyro bias during the measurement, which combines the turn-on repeatability, the residual of any calibration, and the drift during the run. It is not the in-run bias instability that datasheets often quote, which can be several times smaller. The first term decreases with the averaging time, and the second does not. The two are equal at the crossover time

$$T_c = \left(\frac{N_E}{\sigma_{bg}} \right)^2 , \tag{19}$$

beyond which longer averaging brings little benefit. For $T \gg T_c$ the heading accuracy is limited by the gyro bias stability. All terms grow toward the poles, the gyro terms as $1/\cos L$ and the accelerometer term as $\tan L$. A well-known way to remove the bias term is to repeat the measurement after rotating the IMU by 180° about the vertical, which reverses the sign of the bias-induced error while it preserves the Earth-rate signal. The remainder of this paper considers a single orientation.

4 Sensor Requirements

Eq. (18) answers the practical question of which sensor quality a north finder needs. Suppose that a heading accuracy σ^* is required within the alignment time T and that the budget is shared equally between the noise and the bias terms. Each of the two terms may then contribute $\sigma^*/\sqrt{2}$, which gives

$$\sigma_{bg} \le \frac{\sigma^*}{\sqrt{2}} \, \Omega \cos L, \qquad N_E \le \frac{\sigma^*}{\sqrt{2}} \, \Omega \cos L \, \sqrt{T}, \qquad \sigma_{ba} \ll \frac{g \, \sigma^*}{\tan L}. \tag{20}$$

Table 1 evaluates (20) at $L = 40.92°$. A heading accuracy of 1° requires a bias stability of about 0.14°/h and, for a one-minute alignment, an angle random walk of about $0.018°/\sqrt{\text{h}}$. An accuracy of 0.1° requires ten times better values. The accelerometer requirement is mild. Even for 0.1°, the accelerometer term alone would consume the whole budget only at a bias of 2 mg.

Table 1. Gyro requirements for a heading accuracy σ^* (1σ) at $L = 40.92°$, with the budget shared equally between noise and bias according to (20).

Heading accuracy σ^*	Bias stability σ_{bg}	Angle random walk N_E	
		$T = 60$ s	$T = 600$ s
1°	0.14°/h	$0.018°/\sqrt{\text{h}}$	$0.057°/\sqrt{\text{h}}$
0.5°	0.070°/h	$0.0091°/\sqrt{\text{h}}$	$0.029°/\sqrt{\text{h}}$
0.1°	0.014°/h	$0.0018°/\sqrt{\text{h}}$	$0.0057°/\sqrt{\text{h}}$

Table 2 and Fig. 2 show the accuracy that representative sensor grades achieve, using typical bias stabilities and noise densities of each class [7, 15]. A navigation-grade IMU reaches a few hundredths of a degree within minutes. A high-end tactical-grade IMU, the class of the FOG unit used in Section 7, reaches about 0.6° in one minute and is bias-limited at 0.5°. Its crossover time (19) is about half a minute, so averaging much longer than a few minutes is of little use. A tactical-grade unit with a 1°/h bias cannot do better than 5°, and industrial-grade sensors with biases of 10°/h or more cannot find north by static gyrocompassing at all. Sub-degree north finding within minutes therefore requires gyroscopes with a bias stability of about 0.1°/h or better and an angle random walk of about $0.01°/\sqrt{\text{h}}$, which is the domain of fiber-optic and ring-laser gyroscopes. Under quasi-stationary conditions the angular motion of the support appears in the gyro outputs as additional noise, and in the experiment of Section 7 it doubles the apparent angle random walk of the horizontal gyros. A genuine rotation of the support is followed by the strapdown filter and is no error for it, but the noise identification cannot always separate the two, so a margin on the noise requirement is prudent.

Table 2. Heading accuracy (1σ) of static gyrocompassing for representative sensor grades at $L = 40.92°$ according to (18), with the same N on all axes so that $N_E = N$. The limit is the value for $T \to \infty$. For the industrial grade the linearized budget overstates the error, the exact heading error of a $10°/\mathrm{h}$ east bias being $41°$.

Grade	σ_{bg}	N	σ_{ba}	σ_ψ after T			Limit
	$(°/\mathrm{h})$	$(°/\sqrt{\mathrm{h}})$	(mg)	60 s	300 s	600 s	
Navigation	0.005	0.002	0.05	0.082°	0.043°	0.035°	0.025°
High-end tactical	0.1	0.01	0.5	0.64°	0.53°	0.52°	0.50°
Tactical	1	0.1	1	6.4°	5.3°	5.2°	5.0°
Industrial	10	0.3	5	52°	51°	51°	50°

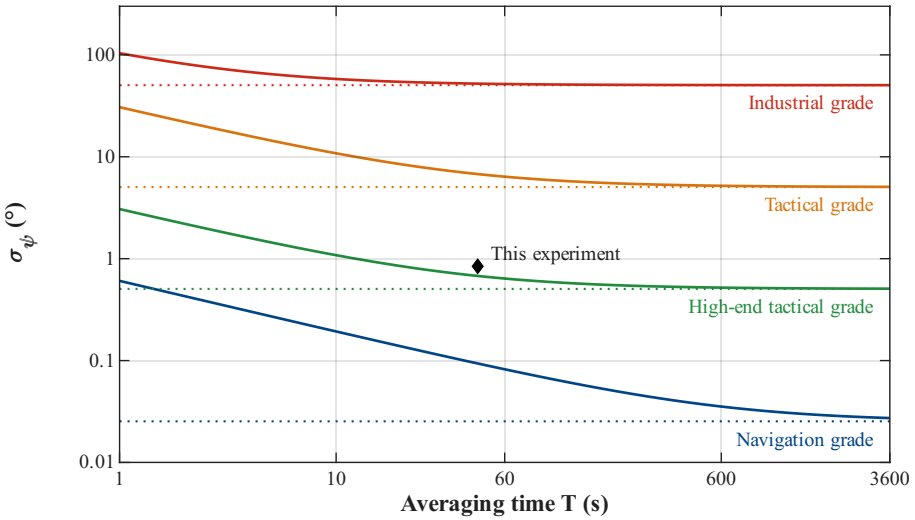


Figure 2. Heading accuracy (1σ) of static gyrocompassing versus averaging time for representative sensor grades at $L = 40.92°$ according to (18). Dotted lines show the bias limits, and the diamond marks the analytic gyrocompass of the experiment in Section 7 ($T = 45\,\mathrm{s}$, $N_E = 0.0149°/\sqrt{\mathrm{h}}$).

5 Sensor Noise Identification

The noise densities in (18) and in the process noise of the filter must be identified from data. This section describes two complementary tools for this purpose.

5.1 Stochastic error model

The error of a gyro or accelerometer output is commonly modeled as the sum of a constant bias, white noise, bias instability (flicker noise), and a random walk of the bias [5, 9]. White rate noise integrates into an angle random walk (ARW) with density N, usually quoted in $°/\sqrt{\mathrm{h}}$. For accelerometers the corresponding velocity random walk (VRW) is quoted in $\mu\mathrm{g}/\sqrt{\mathrm{Hz}}$. The bias instability B describes the slow wandering of the bias, and the rate random walk K describes its long-term drift. Over the short records of a north-finding measurement, white noise and the bias dominate.

5.2 Allan variance

Let $\tilde{\omega}_j$, $j = 1, \ldots, M$, be the output samples taken at the interval T_s, let $\Theta_k = T_s \sum_{j<k} \tilde{\omega}_j$ be the integrated output (an angle for a gyro), and let $\tau = mT_s$ be the cluster time. The overlapping Allan variance [1, 9] is

$$\sigma^2(\tau) = \frac{1}{2\tau^2 (M - 2m + 1)} \sum_{k=1}^{M-2m+1} \left(\Theta_{k+2m} - 2\Theta_{k+m} + \Theta_k\right)^2. \tag{21}$$

It is related to the two-sided power spectral density $S_\omega(f)$ of the rate by

$$\sigma^2(\tau) = 4\int_0^\infty S_\omega(f)\,\frac{\sin^4(\pi f\tau)}{(\pi f\tau)^2}\,\mathrm{d}f, \tag{22}$$

so that each noise type has its own slope on a log-log plot. White noise gives $\sigma(\tau) = N/\sqrt{\tau}$ with slope $-1/2$, bias instability gives a flat floor $\sigma \approx 0.664\,B$, and rate random walk gives $\sigma = K\sqrt{\tau/3}$ with slope $+1/2$ [5, 9]. The ARW is read at $\tau = 1$ s on the $-1/2$ slope. Since $1°/\sqrt{\mathrm{h}}$ equals $60\,(°/\mathrm{h})/\sqrt{\mathrm{Hz}}$, the gyro Allan deviation at $\tau = 1$ s in °/h divided by 60 gives N in $°/\sqrt{\mathrm{h}}$. The relative uncertainty of an Allan deviation computed from M samples with cluster size m is about $1/\sqrt{2(M/m-1)}$ [5]. For the 45 s span of a one-minute record it is about 11 % at $\tau = 1$ s but 50 % at $\tau = 15$ s, so the bias instability, which appears at long cluster times, cannot be resolved from a short record.

5.3 Power spectral density

The Allan variance mixes all frequencies through the kernel of (22), and narrow-band components such as structural resonances of the support leave bumps in it. The power spectral density separates them. It is estimated with Welch's method [17]. The record is split into segments with 50 % overlap, the mean of each segment is removed, each segment is weighted by a Hann window, and the squared magnitudes of their Fourier transforms are averaged. The result is the one-sided density $G(f)$, which equals $2N^2$ for white noise of density N. This paper therefore plots $\sqrt{G(f)/2}$, so that white noise appears at the level N. The square of the white-noise density, N^2, is estimated as the mean of $G(f)/2$ over a low-frequency band free of resonances, here the frequency bins from 0.098 to 0.977 Hz of segments with 4096 samples, which this paper calls the band from 0.1 to 1 Hz. This is the lowest band that a short record resolves reliably and the closest to the very low frequencies on which the mean rate of a north-finding measurement depends.

5.4 From noise densities to filter noise

For the filter of Section 6, white noise of density N_i on body axis i produces over one step T_s an attitude error with variance $N_i^2 T_s$ about that axis. Resolved in NED axes, the per-step process noise of the attitude error is $\mathbf{C}_b^n\,\mathrm{diag}(N_1^2, N_2^2, N_3^2)\,(\mathbf{C}_b^n)^\top T_s$, and that of the velocity error is formed in the same way from the accelerometer densities.

6 Quaternion Error-State Kalman Filter

Analytic gyrocompassing uses only averages and therefore treats the disturbing motion and the noise alike. The fine-alignment filter described in this section propagates the full strapdown solution, uses the zero-velocity knowledge as a measurement, estimates the sensor biases and the disturbance, and provides an uncertainty of the heading at every instant. It is an error-state filter. A nominal state is propagated with the bias-corrected IMU data, and a Kalman filter estimates the small error of the nominal state, which is fed back after each measurement [7, 14]. Algorithm 1 summarizes the complete procedure.

6.1 Nominal state and strapdown propagation

The nominal state consists of the attitude quaternion $\hat{\mathbf{q}}$, the NED velocity $\hat{\boldsymbol{v}}$ and displacement $\hat{\boldsymbol{r}}$ from the starting point, the accumulated bias estimates $\hat{\boldsymbol{b}}_a$ and $\hat{\boldsymbol{b}}_g$, and the estimate $\hat{\boldsymbol{d}} = [\hat{d}_N,\ \hat{d}_E]^\top$ of the horizontal specific-force disturbance. At each IMU sample k, the bias-corrected measurements are $\hat{\boldsymbol{\omega}}_k = \tilde{\boldsymbol{\omega}}_k - \hat{\boldsymbol{b}}_g$ and $\hat{\boldsymbol{f}}_k = \tilde{\boldsymbol{f}}_k - \hat{\boldsymbol{b}}_a$. The attitude advances by the body rotation $\hat{\boldsymbol{\omega}}_k T_s$ relative to inertial space, applied on the right, and by the rotation $-\boldsymbol{\omega}_{ie}^n T_s$ of the navigation frame, which turns with the Earth, applied on the left,

$$\hat{\mathbf{q}}_k = \mathbf{q}\big(-\boldsymbol{\omega}_{ie}^n T_s\big) \otimes \hat{\mathbf{q}}_{k-1} \otimes \mathbf{q}\big(\hat{\boldsymbol{\omega}}_k T_s\big), \qquad \hat{\mathbf{q}}_k \leftarrow \hat{\mathbf{q}}_k / \|\hat{\mathbf{q}}_k\|. \tag{23}$$

With $\hat{\mathbf{C}}_k = \mathbf{C}(\hat{\mathbf{q}}_k)$, the velocity, displacement, and disturbance follow as

$$\hat{\boldsymbol{v}}_k = \hat{\boldsymbol{v}}_{k-1} + \big[\tfrac{1}{2}\big(\hat{\mathbf{C}}_k + \hat{\mathbf{C}}_{k-1}\big)\hat{\boldsymbol{f}}_k - \mathbf{E}\hat{\boldsymbol{d}}_{k-1} + \boldsymbol{g}^n\big]\,T_s, \tag{24}$$

$$\hat{\boldsymbol{r}}_k = \hat{\boldsymbol{r}}_{k-1} + \tfrac{1}{2}\big(\hat{\boldsymbol{v}}_{k-1} + \hat{\boldsymbol{v}}_k\big)T_s, \tag{25}$$

$$\hat{\boldsymbol{d}}_k = e^{-T_s/\tau_d}\,\hat{\boldsymbol{d}}_{k-1}, \tag{26}$$

where $\mathbf{E} = [\mathbf{I}_2,\ \mathbf{0}]^\top$ maps the north and east disturbance into NED and τ_d is the correlation time of the disturbance model (Section 6.2). The Coriolis term $-2\boldsymbol{\omega}_{ie}^n \times \boldsymbol{v}$ and the transport rate are omitted. At the residual speed of a quasi-stationary IMU, below 10^{-4} m/s, they are below 2×10^{-8} m/s^2 and $10^{-5}\,^\circ$/h, many orders of magnitude below the sensor errors. The Earth rate itself is retained in (23) because it is the signal of gyrocompassing.

6.2 Error state and its dynamics

The error state has 17 components,

$$\delta\boldsymbol{x} = \left[\delta\boldsymbol{\psi}^\top,\ \delta\boldsymbol{v}^\top,\ \delta\boldsymbol{r}^\top,\ \delta\boldsymbol{b}_a^\top,\ \delta\boldsymbol{b}_g^\top,\ \delta\boldsymbol{d}^\top\right]^\top. \tag{27}$$

The attitude error $\delta\boldsymbol{\psi}$ is a small rotation vector in NED axes defined by $\mathbf{C}_b^n = \mathbf{C}(\mathbf{q}(-\delta\boldsymbol{\psi}) \otimes \hat{\mathbf{q}}) \approx (\mathbf{I} - [\,\delta\boldsymbol{\psi}\times])\hat{\mathbf{C}}_b^n$, so that $\delta\psi_D$ is the heading error. The velocity and displacement errors are $\delta\boldsymbol{v} = \hat{\boldsymbol{v}} - \boldsymbol{v}$ and $\delta\boldsymbol{r} = \hat{\boldsymbol{r}} - \boldsymbol{r}$. The bias and disturbance states are the residuals not yet compensated, $\delta\boldsymbol{b} = \boldsymbol{b} - \hat{\boldsymbol{b}}$ and $\delta\boldsymbol{d} = \boldsymbol{d} - \hat{\boldsymbol{d}}$. For a stationary IMU the errors obey [7, 15]

$$\delta\dot{\boldsymbol{\psi}} = -[\,\boldsymbol{\omega}_{ie}^n\times]\delta\boldsymbol{\psi} + \hat{\mathbf{C}}_b^n\,\delta\boldsymbol{b}_g + \hat{\mathbf{C}}_b^n\boldsymbol{w}_g, \tag{28}$$

$$\delta\dot{\boldsymbol{v}} = -[\,\boldsymbol{f}^n\times]\delta\boldsymbol{\psi} + \mathbf{C}_0\,\delta\boldsymbol{b}_a + \mathbf{E}\,\delta\boldsymbol{d} + \hat{\mathbf{C}}_b^n\boldsymbol{w}_a, \tag{29}$$

$$\delta\dot{\boldsymbol{r}} = \delta\boldsymbol{v}, \qquad \delta\dot{\boldsymbol{b}}_a = \boldsymbol{w}_{ba}, \qquad \delta\dot{\boldsymbol{b}}_g = \boldsymbol{w}_{bg}, \qquad \delta\dot{\boldsymbol{d}} = -\delta\boldsymbol{d}/\tau_d + \boldsymbol{w}_d. \tag{30}$$

Two choices adapt the model to the quasi-stationary case. First, the specific force in (29) is the static value $\boldsymbol{f}^n = [0,\ 0,\ -g]^\top$ rather than the measured one, so that vibration does not enter the coupling between attitude and velocity errors. Second, the accelerometer bias, which is fixed to the body, is mapped into NED with the initial attitude $\mathbf{C}_0$ rather than with the current estimate. The attitude of a stationary IMU is constant, and evaluating the Jacobian at a fixed point, known as a first-estimate Jacobian [8], keeps the filter from attributing the slow motion of the heading estimate to the horizontal accelerometer biases, which are not observable (Section 6.7). The disturbance $\boldsymbol{d}$ is a first-order Gauss-Markov process with correlation time τ_d and standard deviation σ_d. It models a correlated error of the measured horizontal specific force that does not correspond to a change of velocity, such as the part of the rocking of the support that the strapdown attitude does not follow. The translation of the support itself is covered by the noise of the zero-velocity measurement (Section 6.4). In compact form $\delta\dot{\boldsymbol{x}} = \mathbf{F}\delta\boldsymbol{x} + \mathbf{G}\boldsymbol{w}$, where $\boldsymbol{w} = [\boldsymbol{w}_g^\top, \boldsymbol{w}_a^\top, \boldsymbol{w}_{ba}^\top, \boldsymbol{w}_{bg}^\top, \boldsymbol{w}_d^\top]^\top$ collects the white noises and $\mathbf{G}$ is their input matrix, with

$$\mathbf{F} = \begin{bmatrix} -[\,\boldsymbol{\omega}_{ie}^n\times] & \mathbf{0} & \mathbf{0} & \mathbf{0} & \hat{\mathbf{C}}_b^n & \mathbf{0} \\ -[\,\boldsymbol{f}^n\times] & \mathbf{0} & \mathbf{0} & \mathbf{C}_0 & \mathbf{0} & \mathbf{E} \\ \mathbf{0} & \mathbf{I}_3 & \mathbf{0} & \mathbf{0} & \mathbf{0} & \mathbf{0} \\ \mathbf{0} & \mathbf{0} & \mathbf{0} & \mathbf{0} & \mathbf{0} & \mathbf{0} \\ \mathbf{0} & \mathbf{0} & \mathbf{0} & \mathbf{0} & \mathbf{0} & \mathbf{0} \\ \mathbf{0} & \mathbf{0} & \mathbf{0} & \mathbf{0} & \mathbf{0} & -\mathbf{I}_2/\tau_d \end{bmatrix}. \tag{31}$$

6.3 Discretization and prediction

Over one IMU step the transition matrix is approximated by the third-order series $\boldsymbol{\Phi}_k = \mathbf{I} + \mathbf{A} + \mathbf{A}^2/2 + \mathbf{A}^3/6$ with $\mathbf{A} = \mathbf{F}T_s$, and the process noise covariance is block diagonal,

$$\mathbf{Q}_k = \operatorname{diag}\Big(\hat{\mathbf{C}}_k\mathbf{N}_g\hat{\mathbf{C}}_k^\top T_s,\ \hat{\mathbf{C}}_k\mathbf{N}_a\hat{\mathbf{C}}_k^\top T_s,\ \mathbf{0}_3,\ q_{ba}^2 T_s\mathbf{I}_3,\ q_{bg}\mathbf{I}_3,\ \sigma_d^2\big(1 - e^{-2T_s/\tau_d}\big)\mathbf{I}_2\Big), \tag{32}$$

where $\mathbf{N}_g = \operatorname{diag}(N_{g,1}^2, N_{g,2}^2, N_{g,3}^2)$ and $\mathbf{N}_a = \operatorname{diag}(N_{a,1}^2, N_{a,2}^2, N_{a,3}^2)$ contain the identified noise densities (Section 5), q_{ba} is the accelerometer bias random walk, and q_{bg} is the per-step gyro bias variance. The covariance is predicted as $\mathbf{P}_k^- = \boldsymbol{\Phi}_k\mathbf{P}_{k-1}^+\boldsymbol{\Phi}_k^\top + \mathbf{Q}_k$.

6.4 Zero-velocity measurement and update

The instrument does not move on average, so its true velocity is zero up to the residual motion. The zero-velocity update (ZUPT) uses this knowledge as a pseudo-measurement,

$$\boldsymbol{z}_k = \mathbf{0} - \hat{\boldsymbol{v}}_k = -\delta\boldsymbol{v}_k + \boldsymbol{\eta}_k, \qquad \mathbf{H} = \left[\mathbf{0}_3\ \ -\mathbf{I}_3\ \ \mathbf{0}_3\ \ \mathbf{0}_3\ \ \mathbf{0}_3\ \ \mathbf{0}_{3\times 2}\right], \qquad \mathbf{R} = \sigma_\eta^2\mathbf{I}_3, \tag{33}$$

Algorithm 1 Quasi-stationary north finding with a quaternion error-state Kalman filter

Input IMU samples $\tilde{\boldsymbol{\omega}}_k$ and $\tilde{\boldsymbol{f}}_k$ at the interval T_s, latitude L, height h, noise densities $\mathbf{N}_g$ and $\mathbf{N}_a$, prior standard deviations, and the ZUPT period of $n_u = 1/(f_u T_s)$ samples

Coarse alignment

$\bar{\boldsymbol{f}}, \bar{\boldsymbol{\omega}} \leftarrow$ averages of $\tilde{\boldsymbol{f}}_k$ and $\tilde{\boldsymbol{\omega}}_k$ over the stationary span

$\phi, \theta \leftarrow$ leveling (11) from $\bar{\boldsymbol{f}}$, $\quad \psi \leftarrow$ gyrocompassing (13) from $\bar{\boldsymbol{\omega}}$

$\hat{\mathbf{q}} \leftarrow \mathbf{q}(\psi \boldsymbol{e}_3) \otimes \mathbf{q}(\theta \boldsymbol{e}_2) \otimes \mathbf{q}(\phi \boldsymbol{e}_1)$, $\quad \mathbf{C}_0 \leftarrow \mathbf{C}(\hat{\mathbf{q}})$ ▷ (5)

$\hat{\boldsymbol{v}}, \hat{\boldsymbol{r}}, \hat{\boldsymbol{b}}_a, \hat{\boldsymbol{b}}_g \leftarrow \mathbf{0}_3$, $\quad \hat{\boldsymbol{d}} \leftarrow \mathbf{0}_2$

$\mathbf{P} \leftarrow \operatorname{diag}\left(\sigma_{\psi_N}^2, \sigma_{\psi_E}^2, \sigma_{\psi_D}^2, \sigma_v^2 \mathbf{I}_3, \sigma_r^2 \mathbf{I}_3, \sigma_{ba}^2 \mathbf{I}_3, \sigma_{bg}^2 \mathbf{I}_3, \sigma_d^2 \mathbf{I}_2\right)$

Fine alignment

for $k = 1, 2, \ldots$ **do**

  $\hat{\boldsymbol{\omega}} \leftarrow \tilde{\boldsymbol{\omega}}_k - \hat{\boldsymbol{b}}_g$, $\quad \hat{\boldsymbol{f}} \leftarrow \tilde{\boldsymbol{f}}_k - \hat{\boldsymbol{b}}_a$

  $\hat{\mathbf{C}}^- \leftarrow \mathbf{C}(\hat{\mathbf{q}})$, $\quad \hat{\mathbf{q}} \leftarrow \mathbf{q}(-\boldsymbol{\omega}_{ie}^n T_s) \otimes \hat{\mathbf{q}} \otimes \mathbf{q}(\hat{\boldsymbol{\omega}} T_s)$ ▷ (23)

  $\hat{\mathbf{q}} \leftarrow \hat{\mathbf{q}}/\|\hat{\mathbf{q}}\|$, $\quad \hat{\mathbf{C}} \leftarrow \mathbf{C}(\hat{\mathbf{q}})$

  $\hat{\boldsymbol{v}}^- \leftarrow \hat{\boldsymbol{v}}$, $\quad \hat{\boldsymbol{v}} \leftarrow \hat{\boldsymbol{v}} + \left[\tfrac{1}{2}(\hat{\mathbf{C}} + \hat{\mathbf{C}}^-)\hat{\boldsymbol{f}} - \mathbf{E}\hat{\boldsymbol{d}} + \boldsymbol{g}^n\right] T_s$ ▷ (24)

  $\hat{\boldsymbol{r}} \leftarrow \hat{\boldsymbol{r}} + \tfrac{1}{2}(\hat{\boldsymbol{v}}^- + \hat{\boldsymbol{v}}) T_s$, $\quad \hat{\boldsymbol{d}} \leftarrow e^{-T_s/\tau_d}\, \hat{\boldsymbol{d}}$ ▷ (25) and (26)

  $\mathbf{A} \leftarrow \mathbf{F}(\hat{\mathbf{C}})\, T_s$, $\quad \boldsymbol{\Phi} \leftarrow \mathbf{I} + \mathbf{A} + \mathbf{A}^2/2 + \mathbf{A}^3/6$ ▷ (31)

  $\mathbf{P} \leftarrow \boldsymbol{\Phi}\mathbf{P}\boldsymbol{\Phi}^\top + \mathbf{Q}(\hat{\mathbf{C}})$ ▷ (32)

  if k is a multiple of n_u **then** ▷ zero-velocity update

    $\boldsymbol{z} \leftarrow -\hat{\boldsymbol{v}}$, $\quad \mathbf{S} \leftarrow \mathbf{H}\mathbf{P}\mathbf{H}^\top + \mathbf{R}$, $\quad \mathrm{NIS} \leftarrow \boldsymbol{z}^\top \mathbf{S}^{-1} \boldsymbol{z}$ ▷ (33)

    $\mathbf{K} \leftarrow \mathbf{P}\mathbf{H}^\top \mathbf{S}^{-1}$, $\quad \delta\hat{\boldsymbol{x}} \leftarrow \mathbf{K}\boldsymbol{z}$

    $\mathbf{P} \leftarrow (\mathbf{I} - \mathbf{K}\mathbf{H})\, \mathbf{P}\, (\mathbf{I} - \mathbf{K}\mathbf{H})^\top + \mathbf{K}\mathbf{R}\mathbf{K}^\top$ ▷ (34)

    $\hat{\mathbf{q}} \leftarrow \mathbf{q}(-\delta\hat{\boldsymbol{\psi}}) \otimes \hat{\mathbf{q}}$, $\quad \hat{\mathbf{q}} \leftarrow \hat{\mathbf{q}}/\|\hat{\mathbf{q}}\|$ ▷ (35)

    $\hat{\boldsymbol{v}} \leftarrow \hat{\boldsymbol{v}} - \delta\hat{\boldsymbol{v}}$, $\quad \hat{\boldsymbol{r}} \leftarrow \hat{\boldsymbol{r}} - \delta\hat{\boldsymbol{r}}$

    $\hat{\boldsymbol{b}}_a \leftarrow \hat{\boldsymbol{b}}_a + \delta\hat{\boldsymbol{b}}_a$, $\quad \hat{\boldsymbol{b}}_g \leftarrow \hat{\boldsymbol{b}}_g + \delta\hat{\boldsymbol{b}}_g$, $\quad \hat{\boldsymbol{d}} \leftarrow \hat{\boldsymbol{d}} + \delta\hat{\boldsymbol{d}}$

Output Heading $\hat{\psi} = \operatorname{atan2}\big(2(\hat{q}_0\hat{q}_3 + \hat{q}_1\hat{q}_2),\ 1 - 2(\hat{q}_2^2 + \hat{q}_3^2)\big)$ and its uncertainty $\sigma_\psi = \sqrt{P_{33}}$

applied at the rate f_u, which is lower than the IMU rate. The noise $\boldsymbol{\eta}$ represents the residual velocity of the support. Because that motion is correlated over seconds, σ_η is chosen larger than its amplitude. Otherwise successive updates would be treated as independent information, and the covariance would become optimistic. The update uses the Joseph form [4],

$$\mathbf{S} = \mathbf{H}\mathbf{P}^-\mathbf{H}^\top + \mathbf{R}, \quad \mathbf{K} = \mathbf{P}^-\mathbf{H}^\top\mathbf{S}^{-1}, \quad \delta\hat{\boldsymbol{x}} = \mathbf{K}\boldsymbol{z}, \quad \mathbf{P}^+ = (\mathbf{I} - \mathbf{K}\mathbf{H})\mathbf{P}^-(\mathbf{I} - \mathbf{K}\mathbf{H})^\top + \mathbf{K}\mathbf{R}\mathbf{K}^\top, \tag{34}$$

and the normalized innovation squared, $\mathrm{NIS} = \boldsymbol{z}^\top\mathbf{S}^{-1}\boldsymbol{z}$, is monitored. For a consistent filter it follows a χ^2 distribution with three degrees of freedom [3].

6.5 Closed-loop reset

After each update the estimated errors are fed back into the nominal state, and the error estimate is reset to zero,

$$\hat{\mathbf{q}} \leftarrow \mathbf{q}(-\delta\hat{\boldsymbol{\psi}}) \otimes \hat{\mathbf{q}},\ \hat{\mathbf{q}} \leftarrow \hat{\mathbf{q}}/\|\hat{\mathbf{q}}\|, \qquad \hat{\boldsymbol{v}} \leftarrow \hat{\boldsymbol{v}} - \delta\hat{\boldsymbol{v}}, \quad \hat{\boldsymbol{r}} \leftarrow \hat{\boldsymbol{r}} - \delta\hat{\boldsymbol{r}}, \quad \hat{\boldsymbol{b}} \leftarrow \hat{\boldsymbol{b}} + \delta\hat{\boldsymbol{b}}, \quad \hat{\boldsymbol{d}} \leftarrow \hat{\boldsymbol{d}} + \delta\hat{\boldsymbol{d}}. \tag{35}$$

The attitude correction is the exact rotation $\mathbf{q}(-\delta\hat{\boldsymbol{\psi}})$ of (2) applied in the navigation frame, consistent with the definition of $\delta\boldsymbol{\psi}$. The covariance is kept unchanged. The exact reset Jacobian differs from the identity by a term proportional to the correction [14], which is neglected, as is common, because the corrections are small after the first seconds.

6.6 Initialization

The nominal attitude is initialized with the analytic solution of Section 3 over the stationary span and converted to a quaternion with (5), which also fixes $\mathbf{C}_0 = \mathbf{C}(\hat{\mathbf{q}}_0)$. The velocity, displacement, bias, and

disturbance estimates start at zero, and the initial covariance is diagonal. Because the analytic heading is computed from the same data that the filter subsequently processes, its uncertainty is set wide, so that the same information is not counted twice. The bias variances follow from the sensor specification, and the tilt prior of 0.05° covers the 0.029° leveling error that the specified accelerometer bias causes (Table 4). The leveling also correlates the tilts with the horizontal accelerometer biases, which this diagonal prior ignores. The effect on the tilt and bias uncertainties is discussed in Section 7.4, and the heading is not affected.

6.7 Observability at a single position

The heading enters the measurements only indirectly, and the structure of (28) and (29) shows how [2, 11]. With $\boldsymbol{f}^n = [0,\ 0,\ -g]^\top$ and the NED components of (6), the horizontal velocity and tilt errors evolve as

$$\delta\dot{v}_N = -g\,\delta\psi_E + \nabla_N + \delta d_N, \qquad \delta\dot{v}_E = g\,\delta\psi_N + \nabla_E + \delta d_E, \tag{36}$$

$$\delta\dot{\psi}_N = -\Omega\sin L\,\delta\psi_E + \varepsilon_N, \qquad \delta\dot{\psi}_E = \Omega\sin L\,\delta\psi_N + \Omega\cos L\,\delta\psi_D + \varepsilon_E, \tag{37}$$

$$\delta\dot{\psi}_D = -\Omega\cos L\,\delta\psi_E + \varepsilon_D, \tag{38}$$

where $\boldsymbol{\nabla} = \mathbf{C}_0\delta\boldsymbol{b}_a$ and $\boldsymbol{\varepsilon} = \hat{\mathbf{C}}_b^n\delta\boldsymbol{b}_g$ are the residual accelerometer and gyro biases in NED. The disturbance enters (36) in the same way as $\boldsymbol{\nabla}$ and is separated from it only through its correlation time. A heading error makes the east tilt grow at the rate $\Omega\cos L\,\delta\psi_D$, and the tilt makes the north velocity grow quadratically in time, $\delta v_N(t) \approx -\frac{1}{2}g\,\Omega\cos L\,\delta\psi_D\,t^2$, which the ZUPTs detect. A 1° heading error produces a velocity error of 10^{-4} m/s within about 5 s. With constant biases and without the disturbance, setting the velocity errors and all their derivatives to zero in (36) to (38) shows that the zero-velocity measurements cannot distinguish three directions of the error state.

- A heading error together with an east gyro bias $\varepsilon_E = -\Omega\cos L\,\delta\psi_D$. The heading uncertainty therefore cannot fall below $\sigma_{bg}/(\Omega\cos L)$, the gyro-bias term of (18).
- A north tilt together with an east accelerometer bias $\nabla_E = -g\,\delta\psi_N$ and a heading error $\delta\psi_D = -\tan L\,\delta\psi_N = \tan L\,\nabla_E/g$. This is the accelerometer term of (18).
- An east tilt together with a north accelerometer bias $\nabla_N = g\,\delta\psi_E$ and gyro biases $\varepsilon_N = \Omega\sin L\,\delta\psi_E$ and $\varepsilon_D = \Omega\cos L\,\delta\psi_E$. These gyro biases are only Ω times the tilt, about 0.01°/h for a tilt of 0.05°, far below the bias prior, so the east tilt and the north accelerometer bias are separated only through their priors.

All other directions are observable. The north gyro bias makes the north tilt grow linearly and the east velocity quadratically, so it is observable over time, with a resolution limited by the angle random walk. The vertical gyro bias acts only through the heading drift and is weakly observable over a short span. The vertical accelerometer bias drives the down velocity directly and is observable together with the error of the gravity model (7). With the same noise densities, the heading uncertainty of the filter therefore follows the analytic budget and approaches its gyro-bias limit, below which it cannot fall. The benefits of the filter are the treatment of the disturbing motion, the estimation of the observable biases, and an uncertainty of the heading at every instant.

7 Experimental Results

7.1 Experimental setup and data

The IMU is an IFOS-500 [10], which combines three closed-loop interferometric fiber-optic gyroscopes and three pendulous accelerometers in one housing. Its specification lists a gyro bias stability of 0.1°/h at constant temperature and 0.3°/h over the range from −40 to +60°C, an angle random walk of $0.007°/\sqrt{\text{h}}$, an accelerometer bias stability of 0.5 mg, and a velocity random walk of $20\,\mu\text{g}/\sqrt{\text{Hz}}$. The unit stood on a fixed support at latitude 40.92° N and recorded 60 s of data at 200 Hz. The support is a typical quasi-stationary environment. It is still on average but transmits small vibrations to the instrument.

The housing was mounted with its X_s axis pointing down, and the heading reference is the $-Y_s$ axis of the housing. The body frame of Section 2 is therefore $x_b = -Y_s$, $y_b = -Z_s$, $z_b = X_s$. The gyros follow

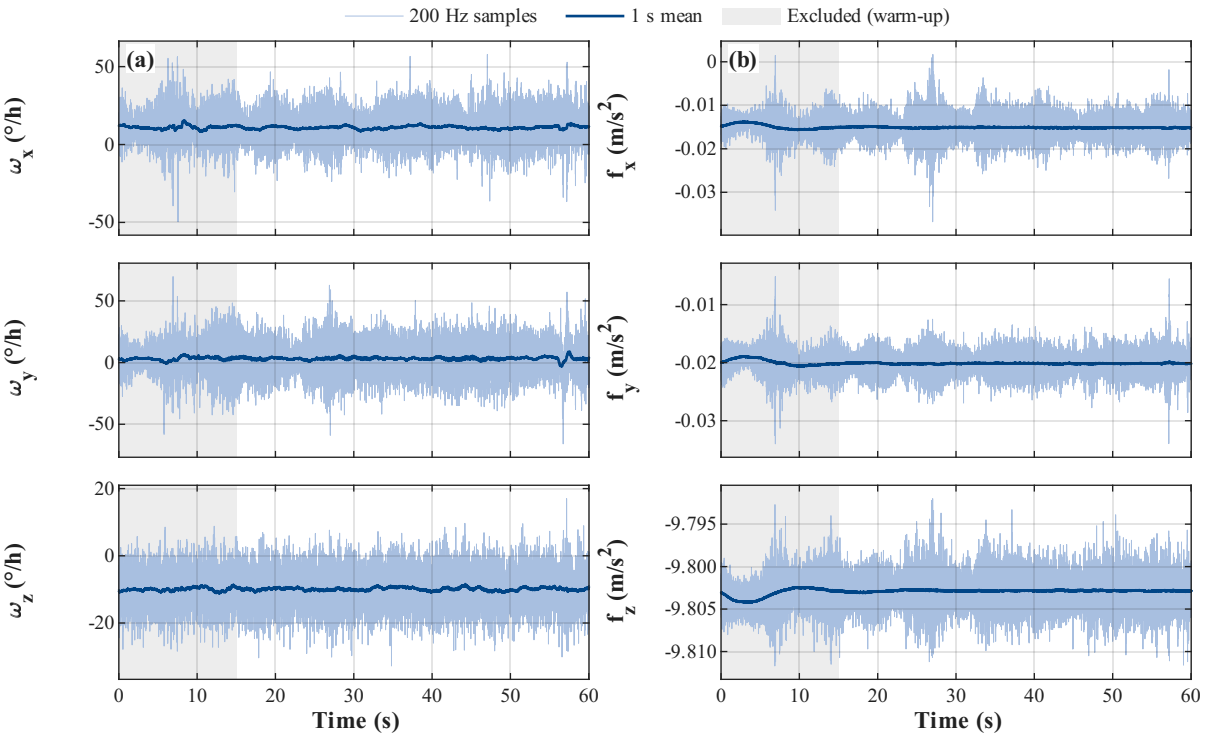


Figure 3. IMU record in body axes for (a) the gyroscopes and (b) the accelerometers. Light lines show the 200 Hz samples and dark lines the 1 s moving means. The shaded first 15 s contain the accelerometer warm-up transient and are excluded from the estimation.

the right-hand rule, whereas the accelerometer channels report the negative of the specific force and thus read $+g$ on an axis pointing down. The body-frame measurements are

$$\tilde{\boldsymbol{\omega}}^b = \mathbf{M}\,\tilde{\boldsymbol{\omega}}^s, \qquad \tilde{\boldsymbol{f}}^b = -\mathbf{M}\,\tilde{\boldsymbol{a}}^s, \qquad \mathbf{M} = \begin{bmatrix} 0 & -1 & 0 \\ 0 & 0 & -1 \\ 1 & 0 & 0 \end{bmatrix}, \tag{39}$$

where $\tilde{\boldsymbol{\omega}}^s$ and $\tilde{\boldsymbol{a}}^s$ are the raw outputs in housing axes. The record contained one empty sample, which was removed, and one corrupted accelerometer sample, which a median-based outlier test replaced by the next valid sample.

Figure 3 shows the record in body axes. After the warm-up the gyro samples scatter with standard deviations of 10.6, 14.0, and 5.7°/h around their means, which are the projections of the Earth rate. During the first 15 s the 1 s means of all three accelerometers show a common transient of up to 0.14 mg, after which they remain within 0.034 mg. This warm-up span is excluded, and all estimates below use the remaining 45 s unless stated otherwise.

7.2 Noise identification

Figures 4 and 5 show the Allan deviations and the noise densities over the 45 s span, and Table 3 lists the identified white-noise levels. The noise densities reveal narrow-band components at 5.37 Hz, 10.84 Hz, about 20 Hz, and about 52 Hz, most likely structural resonances of the support, and a line just below the Nyquist frequency of 100 Hz. These components dominate the sample-to-sample scatter but average out over the alignment. A white-noise level derived from the sample variance would therefore misrepresent the noise that matters for north finding. Below 1 Hz the gyro spectra are nearly flat. On the x and z gyros the floor agrees with the Allan deviation at $\tau = 1$ s to within 12 %, about the uncertainty of the latter. On the y gyro, which carries the strongest resonance, the Allan deviation at 1 s is inflated by it, which illustrates why the spectral view is needed. The accelerometer spectra fall by a factor of two to three between 0.1 and 0.5 Hz and show further components between 1.3 and 2.3 Hz, so their Allan deviations at

1 s exceed the floor by 24 to 72 %.

Table 3. White-noise densities identified from the 45 s analysis span and from the full record, the values adopted for the filter, and the specification. The PSD floor is the mean over the frequency bins from 0.098 to 0.977 Hz of 4096-sample segments.

	Gyro ARW (°/√h)			Accelerometer VRW (µg/√Hz)		
Estimate	x	y	z	x	y	z
45 s analysis span						
Allan deviation at $\tau = 1$ s	0.0114	0.0220	0.0061	7.9	5.6	4.8
PSD floor from 0.1 to 1 Hz	0.0111	0.0126	0.0068	4.6	4.2	3.9
Full 60 s record						
Allan deviation at $\tau = 1$ s	0.0137	0.0212	0.0065	11.2	9.5	9.6
PSD floor from 0.1 to 1 Hz	0.0151	0.0160	0.0070	11.5	10.8	11.0
Adopted	0.0140	0.0150	0.0069	6.9	5.7	4.3
Specification		≤ 0.007			≤ 20	

The Allan deviations in Fig. 4 show the same resonances in another form. A sinusoidal rate of frequency f_0 adds a bump to the Allan deviation that peaks at $\tau \approx 0.37/f_0$ [9], which is about 0.07 s for the line at 5.37 Hz and 0.02 s for the lines near 20 Hz. The y gyro, which carries the strongest resonance, accordingly stays well above its white-noise line between 0.03 and 0.3 s. The accelerometer curves lie above the white-noise model at short cluster times for the same reason and approach it near 1 s. On the x gyro the deviation levels off at about 0.6°/h between 2 and 7 s, above the white-noise line, and the accelerometer deviations rise to about twice their white-noise lines in the same range. Read as bias instability, the gyro plateau would mean about 0.9°/h, nine times the specified value, so a slow motion of the support is the more likely cause, although a one-minute record cannot prove it.

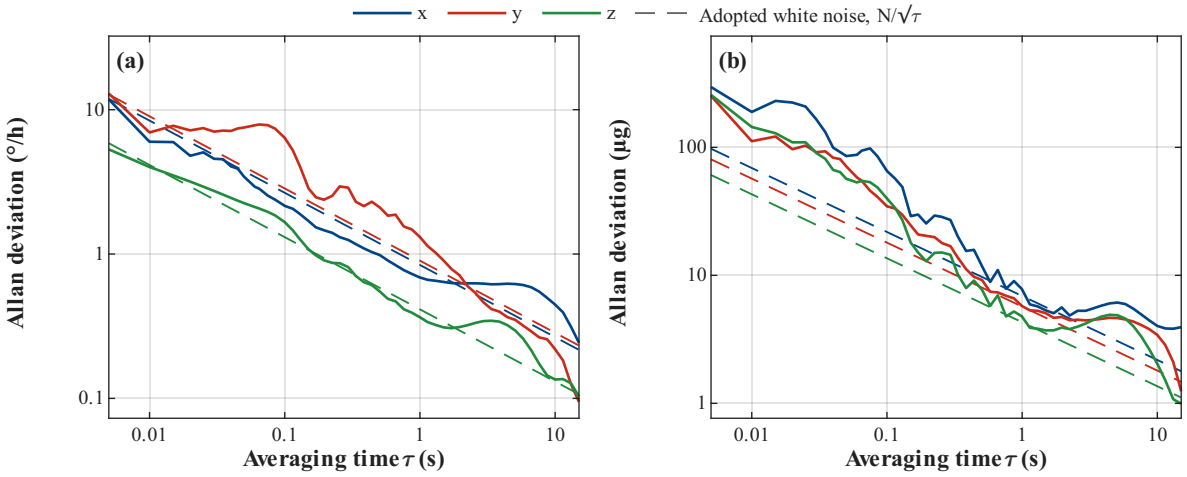


Figure 4. Allan deviations over the 45 s analysis span for (a) the gyroscopes and (b) the accelerometers. Dashed lines show the white-noise model $N/\sqrt{\tau}$ with the adopted densities of Table 3.

The vertical gyro shows 0.006 to 0.007°/√h, close to the specified value. The two horizontal gyros show 1.6 to 3.1 times the specified value, from 0.011 to 0.022°/√h depending on the estimator. The excess appears only on the horizontal axes, which also carry the strongest resonances. This points to angular motion of the support about horizontal axes, in other words to the quasi-stationary disturbance, rather than to sensor noise. The accelerometers show 4 to 8 µg/√Hz, well within the specification. The Allan deviations still decrease at the longest cluster time of 15 s, so the bias instability cannot be resolved from this record, and the specified bias stability is used for the bias priors.

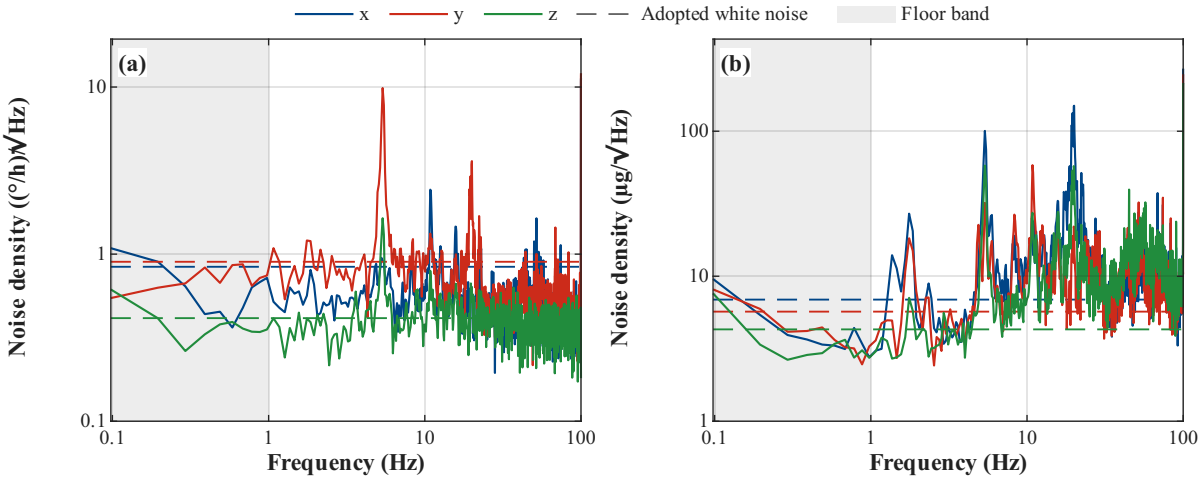


Figure 5. Noise densities $\sqrt{G(f)/2}$ over the 45 s analysis span for (a) the gyroscopes and (b) the accelerometers, computed by Welch's method with a Hann window and 2048-sample segments. Dashed lines show the adopted white-noise densities, and the shaded band from 0.1 to 1 Hz is used for the floor estimate.

The estimates over the full 60 s record are higher, except for the Allan value of the y gyro, because they include the warm-up span. The filter uses the adopted densities in Table 3. They are rounded values chosen within the spread of the four estimates on every axis, and Section 7.6 shows that replacing them by the lowest or the highest estimates changes the heading by only 0.01°. They are drawn as dashed lines in Figs. 4 and 5.

7.3 Analytic alignment

Averaging over the 45 s span gives

$$\bar{\boldsymbol{f}} = [-0.0151,\ -0.0201,\ -9.8029]^{\top}\ \mathrm{m/s^2}, \qquad \bar{\boldsymbol{\omega}} = [10.89,\ 3.29,\ -9.90]^{\top}\ ^{\circ}/\mathrm{h}.$$

Leveling (11) yields $\phi = 0.118°$ and $\theta = -0.088°$, and gyrocompassing (13) yields $\psi = 343.13°$. The consistency checks of Section 3 confirm the vertical channels and the relative sign of the gyro and accelerometer outputs. The specific force magnitude of 9.80289 m/s^2 exceeds the model gravity of 9.80249 m/s^2 by only 0.04 mg, and the vertical component of the measured rate, 9.873°/h, corresponds to a latitude of 41.03°, close to the true 40.92°. With the adopted densities projected on the east axis, $N_E = 0.0149°/\sqrt{\mathrm{h}}$, the budget (18) gives $\sigma_\psi = 0.84°$. It is composed of 0.67° from the gyro noise, 0.50° from the gyro bias, and 0.025° from the accelerometer bias. The crossover time (19) is $T_c = 80$ s. Over the 45 s span the gyro noise therefore still dominates, but the bias term is already of comparable size.

7.4 Error-state Kalman filter

The filter processes the 45 s span with the parameters in Table 4. Figure 6(a) shows the heading estimate with its 1σ band. During the first seconds, when the heading uncertainty is still several degrees or more, the estimate moves by several degrees. After about 15 s of data it remains within $\pm 1\sigma$ of its final value,

$$\hat{\psi} = 342.70°, \qquad \sigma_\psi = 0.88°. \tag{40}$$

Figure 6(b) compares the heading uncertainty of the filter with the analytic budget (18) evaluated for the data processed up to each instant. The uncertainty falls from 4.4° after 5 s of data to 2.1° after 10 s, 1.3° after 20 s, and 0.88° after 45 s, which are the times $t = 20$, 25, 35, and 60 s of Fig. 6. It approaches the analytic curve and, like it, the gyro-bias limit of 0.50°. The excursion of several degrees in the first seconds is a consequence of the wide initial heading uncertainty, with which the filter initially discards the information of the analytic heading, and the simulation of Section 7.5 shows the same behavior.

The analytic gyrocompass solution of 343.13° lies 0.43° from the filter estimate. Both solutions use the same data and share the gyro-bias error, so their difference is much smaller than σ_ψ. Its standard

deviation under the model of Table 4 is 0.26° (Section 7.5), and the observed difference corresponds to 1.7 standard deviations. Most of it has an identifiable cause. The filter infers the heading from the drift of the east tilt, which it sees through the north velocity in (36) and (37). A slow change of the north specific force therefore maps into heading as $\delta\psi \approx \dot{f}_N/(g\,\Omega\cos L)$, about 0.023° per µg of change over 45 s, whereas the average used by the analytic solution sees only the mean tilt. Over the 45 s span the north specific force drifts by −16 µg, which accounts for −0.37°, and removing the linear trend of the horizontal specific force moves the filter estimate to 343.07°. An accelerometer drift of this kind biases the filter, whereas a slow tilt of the support, which the gyros sense, biases the average instead, and this record cannot decide between the two.

Table 4. Parameters of the error-state Kalman filter.

Quantity	Symbol	Value
IMU sampling interval	T_s	5 ms
ZUPT rate and standard deviation	f_u, σ_η	10 Hz, 10^{-4} m/s
Initial tilt uncertainty	σ_{ψ_N}, σ_{ψ_E}	0.05°
Initial heading uncertainty	σ_{ψ_D}	30°
Initial velocity and displacement uncertainty	σ_v, σ_r	10^{-2} m/s, 10^{-3} m
Accelerometer and gyro bias uncertainty	σ_{ba}, σ_{bg}	0.5 mg, 0.1°/h
Gyro and accelerometer noise densities	N_g, N_a	Adopted values of Table 3
Accelerometer bias random walk	q_{ba}	10^{-6} m/s$^2/\sqrt{\text{s}}$
Gyro bias variance per step	q_{bg}	10^{-19} (rad/s)^2
Disturbance correlation time and standard deviation	τ_d, σ_d	2 s, 6×10^{-5} m/s^2

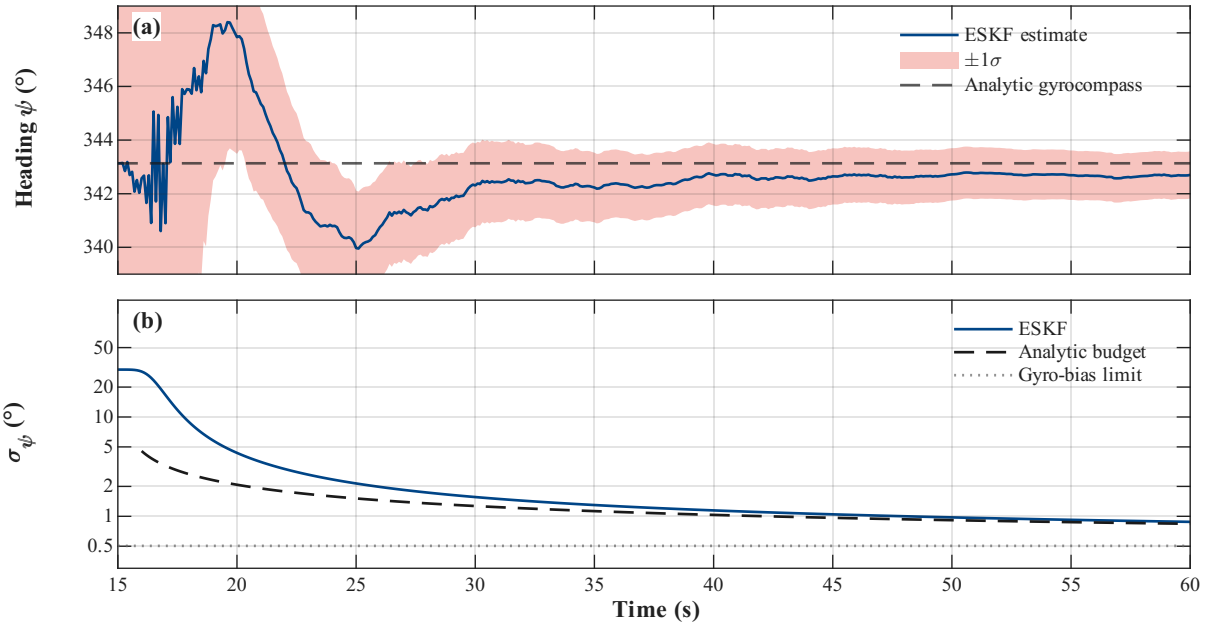


Figure 6. Heading of the body x axis, which is the $-Y_s$ axis of the housing. (a) Filter estimate with its $\pm1\sigma$ band and the analytic gyrocompass solution over the same span. (b) Heading uncertainty of the filter, the analytic budget (18) for the data processed up to each instant, and the gyro-bias limit $\sigma_{bg}/(\Omega\cos L)$.

Figure 7 shows the bias estimates, which confirm the observability analysis of Section 6.7. The body x axis points 17° west of north and the y axis 17° north of east. The uncertainty of the gyro bias on the x axis decreases from 0.10 to 0.083°/h. This bias is observable through the north tilt, but over 45 s the angle random walk limits its resolution to about $N_x/\sqrt{T} = 0.13$°/h, which together with the prior explains the moderate reduction. The gyro biases on the y and z axes remain near their prior at 0.099 and 0.100°/h.

The horizontal accelerometer biases and the tilt angles can only be separated through their priors. The filter determines the combinations $g\,\delta\psi_E - \nabla_N$ and $g\,\delta\psi_N + \nabla_E$ almost exactly. With a wide tilt prior the horizontal biases stay at their prior of 0.5 mg and the tilt uncertainties settle at $\sigma_{ba}/g = 0.029°$, as Section 6.7 predicts. With the tilt prior of Table 4 they come out as 0.43 mg and 0.025°, slightly optimistic because the diagonal prior ignores the correlation that the leveling creates between the tilts and the accelerometer biases. The heading differs by only 0.0005° between the two choices. The vertical accelerometer bias, in contrast, converges to -0.040 ± 0.001 mg. Strictly, this is the bias together with the error of the gravity model (7) at the site, which local anomalies can make tens of µg large. Its agreement with the specific-force check of the analytic alignment, where the measured magnitude exceeded the model gravity by 0.04 mg, is therefore expected rather than independent, since both compare the same data with the same model. Between about 17 and 26 s the estimate departs from its final value by up to 0.016 mg, about five times its σ, probably because the slow vertical motion of the support is not part of the horizontal disturbance model.

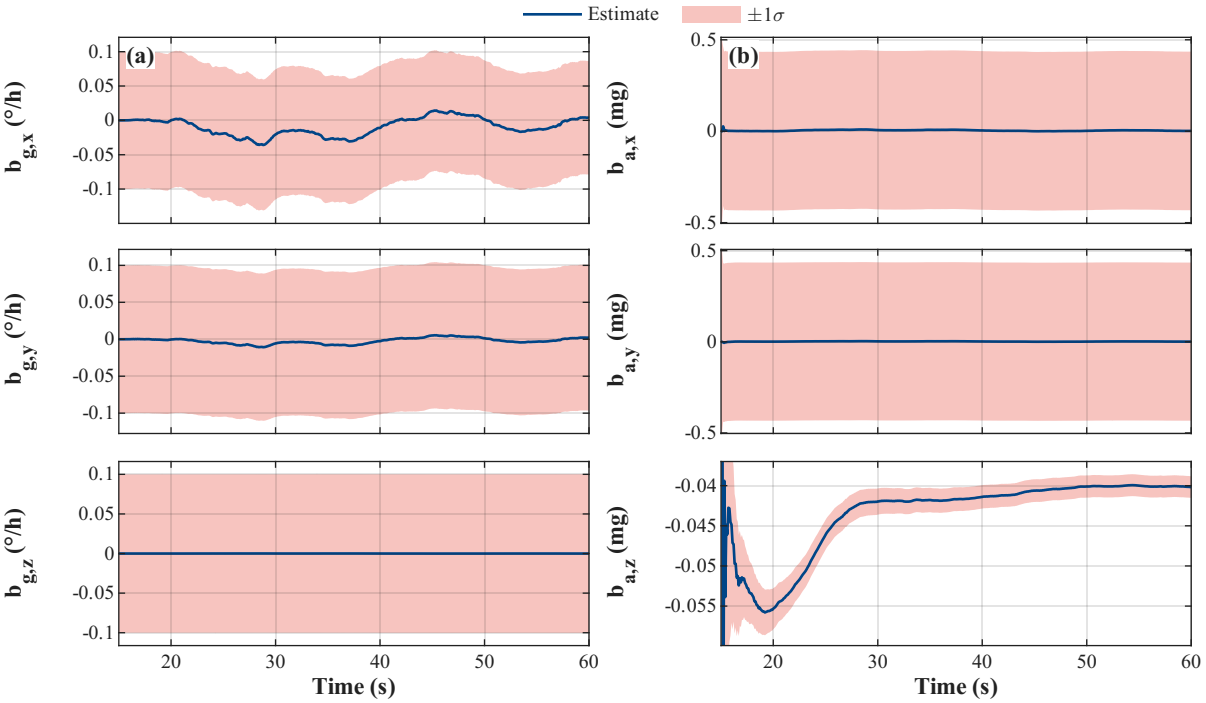


Figure 7. Bias estimates with $\pm 1\sigma$ bands for (a) the gyroscopes and (b) the accelerometers in body axes. The heading reference x_b points 17° west of north and y_b 17° north of east. The vertical axis of the $b_{a,z}$ panel is zoomed to the converged range, so the initial transient from zero is clipped.

Figure 8 shows the normalized innovation squared of the 450 ZUPTs. None exceeds the 95 % bound of the χ^2_3 distribution, and the mean is 0.44, below the expected value of 3. This is the intended consequence of choosing σ_η in (33) larger than the residual motion, and the filter is therefore conservative in velocity. The larger values between 22 and 28 s coincide with a slow vertical motion of the support, during which the estimated down velocity reaches about 0.15 mm/s. The heading is insensitive to the choice of σ_η. Halving it raises the mean NIS to 0.97 and changes the heading by 0.02°, doubling it changes the heading by −0.03°, and σ_ψ changes by less than 0.01° in both cases. The NIS cannot test the heading uncertainty itself, because the heading enters the velocity only in the combination with the east gyro bias that the measurements cannot separate. The realism of σ_ψ rests on the noise densities and the bias prior, and it is checked by simulation in Section 7.5.

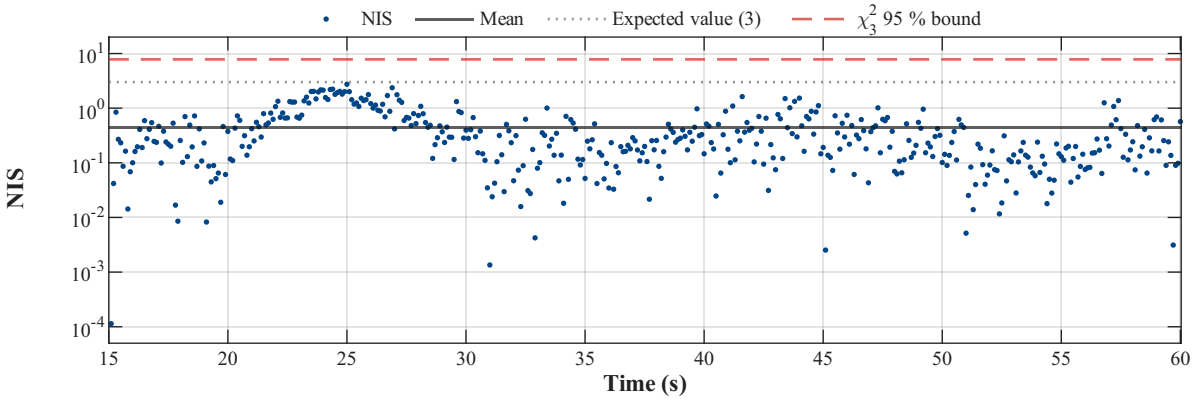


Figure 8. Normalized innovation squared of the zero-velocity updates with its mean, the expected value of the χ^2_3 distribution, and its 95 % bound.

7.5 Monte Carlo simulation

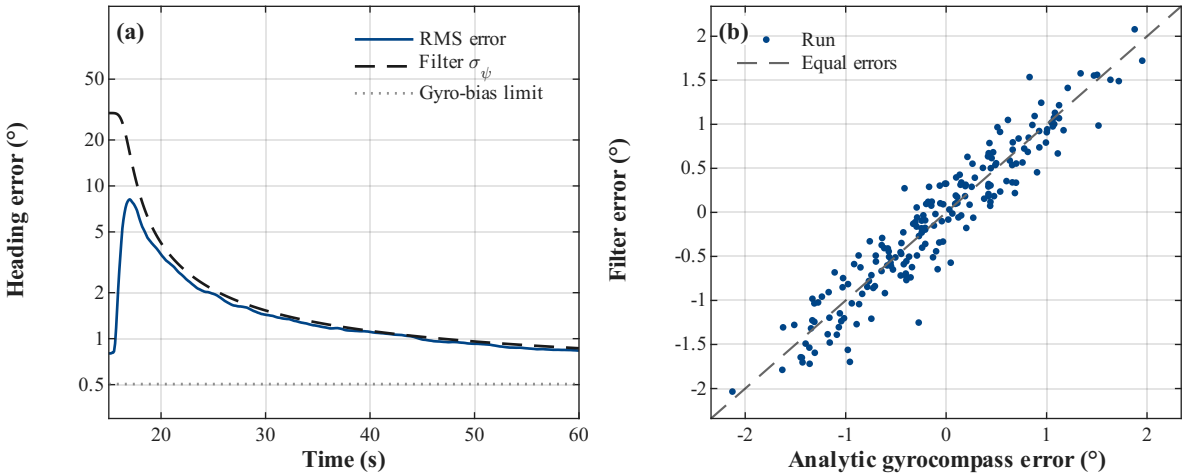


Figure 9. Monte Carlo simulation. (a) RMS heading error over 200 synthetic records with the model of Table 4, the uncertainty σ_ψ predicted by the filter, and the gyro-bias limit. (b) Final heading errors of the filter and of the analytic gyrocompass for each run, with the line of equal errors.

The real record has no reference heading, so the realism of the heading uncertainty is checked by simulation. Each of 200 synthetic records reproduces the time base of the real record and the model of Table 4, with a random true heading, constant biases drawn from the priors, white noise with the adopted densities, and the Gauss-Markov disturbance. The records pass through the same processing as the real data, from the analytic alignment to the filter. Figure 9(a) compares the RMS heading error over the runs with the uncertainty that the filter predicts. Apart from the first seconds, in which the wide initial heading uncertainty makes the filter conservative, the two curves agree, and at the end of the span the RMS value of the normalized error $(\hat{\psi} - \psi)/\sigma_\psi$ is 0.96, close to the value of 1 of a consistent filter. Figure 9(b) compares the final errors of the filter and of the analytic gyrocompass. They are correlated with a coefficient of 0.95 because both share the gyro-bias error. Their standard deviations are 0.83° and 0.80°, while the standard deviation of their difference is only 0.26°. The simulation contains only the effects that the filter models, so it verifies the implementation and the covariance under the assumed model, not the model itself.

7.6 Sensitivity and discussion

Table 5 summarizes the results together with their sensitivity to the modeling choices. Replacing the adopted noise densities by the lowest or the highest estimates of Table 3 on every axis changes the heading

by only 0.01°, far below its uncertainty. The uncertainty σ_ψ ranges from 0.79° to 1.13°, close to the values of 0.76° and 1.09° that (18) predicts for these densities. With the specified $0.007°/\sqrt{\text{h}}$ on all gyro axes the filter gives 342.72° ± 0.63°, because the motion of the support is then no longer treated as gyro noise. A gyro bias uncertainty of 0.3°/h, the specified value over the full temperature range, gives 1.67° and leaves the heading within 0.04°.

Table 5. North-finding results for the heading of the $-Y_s$ axis of the housing with respect to true north, positive clockwise.

Method and configuration	Heading	1σ
Analytic gyrocompass, 45 s	343.13°	0.84°
Quaternion ESKF, 45 s	**342.70°**	**0.88°**
ESKF, lowest noise densities of Table 3	342.71°	0.79°
ESKF, highest noise densities of Table 3	342.71°	1.13°
ESKF, specified gyro noise $0.007°/\sqrt{\text{h}}$ on all axes	342.72°	0.63°
ESKF, σ_η halved	342.72°	0.88°
ESKF, σ_η doubled	342.67°	0.88°
ESKF, gyro bias uncertainty 0.3°/h	342.74°	1.67°

No independent azimuth reference was available during the measurement. The accuracy statement therefore rests on the error budget, whose noise term follows from the noise identification and whose bias term rests on the specification, on the agreement of the filter covariance with this budget, and on the simulation of Section 7.5, which shows that this covariance is realistic under the assumed model. A bias uncertainty larger than the specified 0.1°/h, for example from the turn-on repeatability, would raise the floor proportionally, as the 0.3°/h case shows. Over the 45 s span the gyro noise and the gyro bias contribute 0.67° and 0.50° to the budget. Beyond the crossover time of 80 s the bias dominates, and longer averaging would reduce the uncertainty only toward 0.50°. Further improvement requires a smaller bias, for example through temperature control, or the cancellation of the bias by a second measurement after a 180° rotation about the vertical.

The quasi-stationary disturbances enter in two ways. Their linear part is absorbed by the zero-velocity updates and the disturbance model. Their angular part appears in the gyro outputs as additional noise. A genuine rotation of the support is followed by the strapdown filter and is no error for it, so treating it as white gyro noise is conservative, as the smaller uncertainty with the specified noise density shows. For plain averaging, a bounded rotation of the support adds its net rotation over the span divided by T, which decreases faster than white noise. Finally, the filter is sensitive to a slow drift of the horizontal specific force, which plain averaging is not, so an accelerometer bias drift of a few µg during the measurement is a relevant error source for the filter.

8 Conclusions

This paper developed quasi-stationary north finding from the reference frames to an experimental evaluation. The following conclusions are drawn.

1. Analytic leveling and gyrocompassing follow directly from the measurement model of a stationary IMU. The heading error budget separates the gyro noise, which averages down as $1/\sqrt{T}$, from the gyro bias, which does not and costs 5.04° per 1°/h at 40.92° latitude. A constant accelerometer bias is of minor importance, whereas the filter is sensitive to its drift, about 0.023° per µg over 45 s.

2. The budget translates directly into sensor requirements. Sub-degree north finding within minutes requires a gyro bias stability of about 0.1°/h or better and an angle random walk of about $0.01°/\sqrt{\text{h}}$, which places it in the high-end tactical and navigation grades. Under quasi-stationary conditions the angular motion of the support appears as additional gyro noise, so a margin on the noise requirement is prudent.

3. The Allan variance and the power spectral density are complementary for noise identification. The spectral view separates the resonances of the support from the broadband noise, and the white-noise floor, not the sample variance, should define the process noise of the filter.

4. The quaternion error-state Kalman filter with zero-velocity updates and a Gauss-Markov disturbance model handles quasi-stationary conditions, and a Monte Carlo simulation confirms that its heading uncertainty is realistic under the assumed model. Its accuracy at a single position is bounded by the east gyro bias, as the observability analysis predicts.

5. On a 60 s record of a FOG IMU, the filter estimated the heading as $342.70^\circ \pm 0.88^\circ$, in agreement with the error budget. The analytic gyrocompass gives $343.13^\circ \pm 0.84^\circ$, and the difference is explained by a drift of the north specific force of $-16\,\mu g$ over the span. The heading is insensitive to the noise and measurement parameters within their plausible ranges.

Data and Code Availability

The MATLAB implementation and the IMU record used in this paper are available at https://github.com/RasitEvduzen/KalmanFilter/tree/main/ErrorStateKalmanFilter/QuasiStationaryNorthFinding.

References

[1] D. W. Allan, "Statistics of atomic frequency standards," *Proc. IEEE*, vol. 54, no. 2, pp. 221-230, 1966.

[2] I. Y. Bar-Itzhack and N. Berman, "Control theoretic approach to inertial navigation systems," *J. Guid. Control Dyn.*, vol. 11, no. 3, pp. 237-245, 1988.

[3] Y. Bar-Shalom, X. R. Li, and T. Kirubarajan, *Estimation with Applications to Tracking and Navigation*. Wiley, New York, 2001.

[4] R. S. Bucy and P. D. Joseph, *Filtering for Stochastic Processes with Applications to Guidance*. Interscience, New York, 1968.

[5] N. El-Sheimy, H. Hou, and X. Niu, "Analysis and modeling of inertial sensors using Allan variance," *IEEE Trans. Instrum. Meas.*, vol. 57, no. 1, pp. 140-149, 2008.

[6] J. A. Farrell, *Aided Navigation: GPS with High Rate Sensors*. McGraw-Hill, New York, 2008.

[7] P. D. Groves, *Principles of GNSS, Inertial, and Multisensor Integrated Navigation Systems*, 2nd ed. Artech House, Boston, 2013.

[8] G. P. Huang, A. I. Mourikis, and S. I. Roumeliotis, "Analysis and improvement of the consistency of extended Kalman filter based SLAM," in *Proc. IEEE Int. Conf. Robotics and Automation*, 2008, pp. 473-479.

[9] *IEEE Standard Specification Format Guide and Test Procedure for Single-Axis Interferometric Fiber Optic Gyros*, IEEE Std 952-1997, 1998.

[10] Fiber Optical Solution, *IFOS-500 Inertial Measurement Unit Datasheet*. Riga, Latvia.

[11] Y. F. Jiang and Y. P. Lin, "Error estimation of INS ground alignment through observability analysis," *IEEE Trans. Aerosp. Electron. Syst.*, vol. 28, no. 1, pp. 92-97, 1992.

[12] F. L. Markley, "Attitude error representations for Kalman filtering," *J. Guid. Control Dyn.*, vol. 26, no. 2, pp. 311-317, 2003.

[13] National Imagery and Mapping Agency, "Department of Defense World Geodetic System 1984: Its definition and relationships with local geodetic systems," Tech. Rep. TR8350.2, 3rd ed., 2000.

[14] J. Solà, "Quaternion kinematics for the error-state Kalman filter," arXiv preprint 1711.02508, 2017.

[15] D. H. Titterton and J. L. Weston, *Strapdown Inertial Navigation Technology*, 2nd ed. IEE, London, 2004.

[16] N. Trawny and S. I. Roumeliotis, "Indirect Kalman filter for 3D attitude estimation," Dept. of Computer Science and Engineering, University of Minnesota, Tech. Rep. 2005-002, 2005.

[17] P. D. Welch, "The use of fast Fourier transform for the estimation of power spectra: A method based on time averaging over short, modified periodograms," *IEEE Trans. Audio Electroacoust.*, vol. 15, no. 2, pp. 70-73, 1967.